

Effect of a Shallow Weak Zone on Fault Rupture: Numerical Simulation of Scale-Model Experiments

by Steven M. Day and Geoffrey P. Ely*

Abstract Scale-model earthquake experiments provide detailed, subsurface recordings of rupture propagation and fault motion that are unavailable for natural earthquakes and thereby offer an opportunity to test numerical earthquake simulation methods. Among the advantages realized from the use of experimental data are optimal sensor locations, precise knowledge of bulk and surface properties of the medium, detailed knowledge of the initial stress state, and experimental repeatability. We perform numerical simulations that closely reproduce the shape and duration of the acceleration pulses recorded adjacent to the fault surface in the foam rubber earthquake experiments of Brune and Anooshehpour (1998). Outside of the event nucleation zone, experimental and simulated rupture velocities are nearly indistinguishable. With adjustment of the static friction coefficient within the constraints imposed by experimental measurements, the absolute amplitudes of the accelerations can be brought into close agreement, typically within a few tens of percent. Close agreement between simulation and experiment is also maintained when the frictional strength of the upper part of the fault plane is varied. The agreement of the numerical and experimental results verifies that the discrete numerical model accurately represents the continuum dynamics of the spontaneous rupture problem. The numerical simulations also facilitate further interpretation of the scale-model experiments. They support an interpretation in which fault displacement in the foam experiments occurs predominantly through a conventional frictional sliding mechanism rather than during fault opening episodes, resulting in a cracklike rather than pulselike mode of slip. The simulations further suggest a reinterpretation of the apparent rupture velocity measurements in the fault weak zone, with rupture slowing rather than accelerating. They also predict that the weak zone diminishes surface accelerations and velocities (relative to a uniform fault model) out to a distance that scales with weak-zone depth and may enhance amplitudes slightly at intermediate distances.

Introduction

We simulate numerically the scale-model earthquake experiments of Brune and Anooshehpour (1998). The numerical method simulates spontaneous rupture and frictional sliding on a fault embedded in an elastic continuum. The mathematical formulation and numerical methodology (elastodynamic solver, boundary conditions, fault friction formulation, and spontaneous rupture criterion) are identical to those used in earlier work by Day (1982). Our principal aim is to validate the numerical simulation method, which is based on a finite-difference approximation to the 3D equations of motion.

Comparison with laboratory experiments alone cannot

establish that the formulation of the problem physics upon which our numerical model is based is relevant to real earthquakes. The latter requires modeling of actual earthquake ground-motion recordings. The laboratory experiments nonetheless have the potential to validate the numerical method in several other important respects. At the simplest level, the comparisons serve as an independent check on numerical code logic. Comparisons with the experiments also test the stability and accuracy of the solution algorithm. However, and more fundamentally, the comparisons of laboratory and numerical models provide an independent check on the inherent adequacy of the discrete representation of the continuum that is required in numerical modeling. Such validation is particularly important in nonlinear problems such as this one involving rupture and interface friction.

*Present address: Institute of Geophysics and Planetary Physics, University of California, San Diego, La Jolla, California 92093.

As a means of validating coding, solution algorithms, and ability of discrete systems to approximate the continuum, records from well-controlled laboratory experiments have significant advantages over real earthquake recordings. Strong-motion record sets for earthquakes are sparse and highly aliased spatially, observations are almost exclusively confined to the earth's surface, and the recording sites are usually far removed from the fault plane. The physical scale model experiments of Brune and Anooshehpour (1998), in contrast, permit acceleration time histories to be sampled in the interior of the model, directly adjacent to the simulated fault, and can therefore provide recordings of rupture propagation, slip, and wave motion of a type unavailable for real earthquakes. Furthermore, fault geometry is precisely known in the laboratory model. In addition, model properties such as the wave speeds and friction coefficients are well known through laboratory testing, and initial and final stress states can be measured, limiting the free parameters available to the numerical model. These controlled experiments therefore provide a unique challenge to numerical modeling methodology.

In addition to using comparisons between the physical and numerical models to validate the latter, we use numerical modeling to extend the physical insights obtained from the laboratory experiments. The laboratory model of Brune and Anooshehpour (1998) includes a low frictional-strength surficial layer (weak zone) on the fault. Its purpose is to account in an approximate way for the distinct physical properties and stress state in the upper several kilometers of faults. Brune and Anooshehpour (1998) give a good summary of these physical considerations. Firstly, there are good reasons to expect the shallow zone to be mechanically weak and therefore unable to store and release significant elastic strain energy. Secondly, the presence of thick, unconsolidated gouge layers, as is likely in the near-surface of well-developed faults, may lead to velocity-strengthening frictional behavior (Marone and Scholz, 1988). In that case, shallow slip would occur without a local dynamic stress drop. Alternatively, if a dynamic stress drop does occur in the shallow zone, it may develop gradually, namely, with a low slip-weakening slope, as suggested by Ide and Takeo (1997) on the basis of their space-time slip image of the 1995 Kobe, Japan earthquake. Either way, the shallow slip would be expected to occur at reduced slip velocity (longer rise time).

We use the flexibility and spatiotemporal detail provided by numerical modeling to gain additional insight into the mechanical behaviors seen in the laboratory model, focusing especially on the effects of the weak zone on rupture dynamics and near-fault ground motion. Through numerical modeling, we analyze the propagation of rupture through the weak zone in more detail than is available from the laboratory observations alone. We also examine the distribution of surface motions and their dependence on the depth of the weak zone. Finally, we investigate sensitivities of the rupture behavior to variations in some of the frictional parameters of the model.

Description of the Models

Brune and colleagues have used foam rubber blocks to model a wide range of earthquake processes. Those processes include nucleation, predictability, and rupture mechanism (Brune *et al.*, 1990), interface separation as a possible solution to the heat flow paradox and the paradox of large overthrusts (Brune *et al.*, 1993), and frictional heat generation and seismic radiation (Anooshehpour and Brune, 1994). Physical models of this type provide an opportunity to validate numerical models under well-controlled conditions. The foam rubber model of Brune and Anooshehpour (1998) is particularly relevant to the problem of near-fault ground-motion excitation. It incorporates a weak near-surface layer in the fault zone. The weak layer represents the effects on fault friction caused by the thick gouge that builds up along well-developed natural faults (e.g., Marone, 1998) and which may significantly affect near-fault ground motion. A weak fault layer can also result from thick, surficial deposits of sediments.

The numerical model for this comparative study is a 3D finite-difference model of spontaneous rupture and frictional sliding in an elastodynamic continuum. Three-dimensional finite-difference models of this type have been developed by several investigators (e.g., Miyatake, 1980; Day, 1982; Madariaga *et al.*, 1998). The method used for the current study is that of Day (1982). It was first applied to investigate effects of stress heterogeneity on earthquake rupture dynamics. Subsequent applications have included simulation of the performance of the $m_b:M_s$ seismic discriminant (Stevens and Day, 1985), investigation of earthquake potential on segmented faults (Harris *et al.*, 1991; Harris and Day, 1993, 1999, 2002; Magistrale and Day, 1999), study of the effect of a fault damage zone on rupture propagation and slip (Harris and Day, 1997), and simulation of near-fault seismic directivity pulses (Oglesby and Day, 2002). The numerical treatment of frictional sliding in this numerical model is discussed by Archuleta and Day (1980, appendix) and is compared with an alternative method by Andrews (1999).

Complementarity of Physical and Numerical Earthquake Models

Used together, physical and numerical modeling are complementary approaches to studying earthquake source physics. The physical processes of the foam rubber earthquake model are recorded more completely and in greater detail than is possible for natural events in the earth. The foam model allows independent measurement and control of physical parameters such as normal stress and tectonic loading rate as well as direct measurement of other parameters such as prestress, static stress drop, and friction. In contrast, in numerical simulations of natural earthquakes, these parameters usually must be inferred indirectly from geophysical observations (e.g., geodetic or seismic observations) or simply left as free parameters to be estimated by trial-and-

error fitting of the simulation results to the observations. An additional advantage is that the physical model provides improved observations of the fault slip and ground motion. Sensors can be placed adjacent to the fault plane close to the rupture process, and experiments can be run many times to build large statistical samples. This type of data is valuable for validating the numerical modeling method, and comparable data sets are not available for natural earthquakes. Physical models are also free of the effects of numerical dispersion and spatial resolution limitations that beset numerical models.

However, physical models have certain limitations that a well-validated numerical model is not subject to. Physical models can be affected by artifacts due to (1) artificial boundaries, (2) the finite stiffness of the loading apparatus, and (3) disturbances to the medium such as those caused by the mass and rigidity of embedded sensors. The stiffness of the loading apparatus is not a major issue in the case of the foam rubber model because the loading apparatus can be approximated as infinitely stiff in comparison with the highly compliant foam rubber (Brune and Anooshehpour, 1998). However, the issue is relevant in the case of most rock mechanics experiments. Of the three problems, only artificial boundary effects apply to numerical models. Even then, they can be controlled, for example, either through boundary conditions that absorb most incident energy to mimic an unbounded medium, or simply by greatly extending the computational domain to minimize boundary effects. Additionally, numerical models also allow great flexibility for varying parameters. This allows sensitivity studies to be performed to determine how different parameters influence the rupture process. Numerical models also provide detailed spatial resolution of particle motion which gives a more complete picture of the rupture process than is evident from records at isolated sensors.

Physical Model

The foam rubber model of Brune and Anooshehpour consists of two stacked blocks of foam rubber, each with dimensions $1\text{ m} \times 2\text{ m} \times 2.5\text{ m}$ (Fig. 1). The bottom of the lower block is fixed to the floor, and the system is loaded by slowly shearing the top of the upper block using a piston mounted to the wall. The shearing induces episodic unstable sliding (stick-slip) events along the interface (fault plane) between the blocks. The individual stick-slip events are the model earthquakes that are the focus of this study. The initial normal stress (σ_{n0}) on the fault can be controlled by adjusting the supporting jacks of the upper block, and σ_{n0} was set to 330 Pa (3.3 mbar) for the set of experiments studied here. The upper block was driven at 1 mm/sec by the piston. Characteristic slip events average about 1 cm of slip across the entire fault plane. The objective is to model strike-slip motion on a vertical fault; therefore one of the vertical sides parallel to the drive direction is designated as the ground surface (the ground surface is indicated in Figure 1 by arrows showing relative motion).

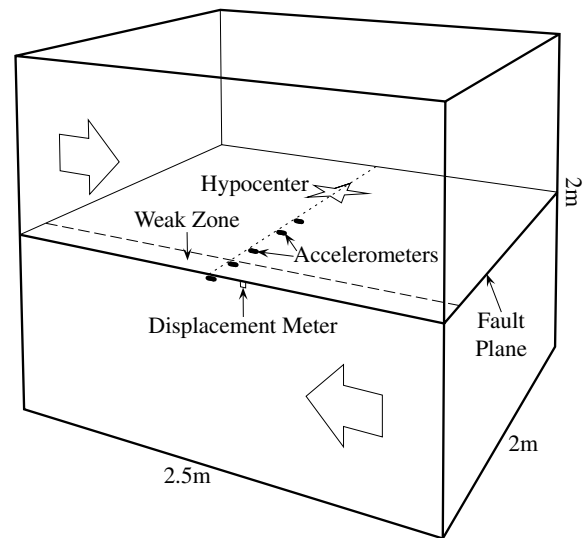


Figure 1. Diagram of Brune and Anooshehpour's (1998) foam rubber model for strike-slip earthquakes. The upper block is forced horizontally past the fixed lower block, inducing stick-slip events along the horizontal fault plane between the blocks. The large arrows are drawn on the surface that represents the free boundary of the earth, and the arrow directions show the sense of relative motion of the two blocks. A weak zone occupies a strip along the top portion of the fault in some of the experiments. The accelerometers record a single component aligned in the fault-strike direction, and they are embedded in the fault wall three centimeters from the fault plane.

An array of five accelerometers is embedded in the fault wall of the lower block at the locations shown in Figure 1. The accelerometers have a single component oriented parallel to the strike of the fault, and they are offset about 3 cm from the fault plane. Also, a displacement sensor located adjacent to the fault trace (at the model ground surface) measures fault slip. The sensor records the displacement of one wall of the fault relative to the fixed external reference frame. Since the stick-slip events are short in duration compared with the time for reloading by the piston motion, shearing displacements of the fault walls are equal in magnitude and opposite in direction during the events. The displacement can therefore be interpreted as a record of one half of the total fault slip.

A force meter was used to record stress on the fault. The average shear prestress (τ_0) measured while the fault was locked up just prior to rupture was 730 Pa (7.3 mbar). The average final stress (τ_f) was 610 Pa (6.1 mbar), giving a static stress drop ($\Delta\tau$) of 120 Pa (1.2 mbar). These values reported by Brune and Anooshehpour (1998) are averages over many events. Some of the events are double events, so the stress drop measurement may be slightly higher than the value for a single event. As an independent check, stress drop can be estimated from the static displacement. For small, uniform slip over the fault plane, $\Delta\tau$ is directly related to final slip s_f

by the formula $\Delta\tau = \rho\beta^2 s_f/L$, where L is the thickness of the model, ρ is density, and β is the S -wave speed. The foam rubber has a density of 16 kg/m^3 , an S -wave speed of 30 m/sec , and a Poisson's ratio of 0.3 . The slip for the particular events that we model is 16 mm , which implies a 120 Pa static stress drop, consistent with the above estimate obtained from force meter measurements.

In some of the earlier foam rubber experiments simulating strike-slip earthquakes (e.g., Brune *et al.*, 1993), slip pulses at a given point on the fault were only a few milliseconds ($\sim 5\text{--}7 \text{ msec}$) in duration, very short compared with the total propagation time of rupture. There is evidence (Brune *et al.*, 1993) supporting an interpretation that, in those experiments, the walls of the fault separate momentarily just behind the rupture front. In that interpretation, all or most of the shear displacement in those earlier experiments occurs while the fault is open and therefore presumably under zero frictional resistance.

The experiments of Brune and Anooshehpour (1998) used in the current study, however, show more conventional frictional sliding behavior. Slip durations at fault points are nearly an order of magnitude greater than in the earlier experiments and are comparable to the full duration of the model earthquake events. The fault walls must remain in frictional contact virtually all of the time during these events. If this were not the case, and the fault were under zero frictional resistance for a significant fraction of the slip duration, then slip velocity, total slip, and stress drop would be all have to be nearly an order of magnitude greater than observed. It is still conceivable that the fault opens very briefly right at the rupture front, though we have no observational evidence one way or the other.

The 1998 experiments, since their dominant mechanism for accommodating shear displacement appears to be frictional sliding, are appropriate analogs for our numerical model. We do not have direct measurements of friction during these events. However, stress measurements just before initiation, and just after cessation, of sliding provide a basis for estimating frictional parameters of the foam, and these estimates are discussed in the Numerical Model section.

To model the weak zone, Brune and Anooshehpour insert strips of plastic into the fault interface along the model ground surface. Where the plastic material is present, the model fault has two important properties that are intended to mimic weak zones in crustal faults. The first is that the coefficient of friction is significantly lower than on the part of the fault with foam surfaces in contact. The second is that the coefficient of friction increases with sliding velocity (velocity strengthening). Rock mechanics experiments have shown that the presence of a thick gouge layer produces similar effects in rock under low confining stress and that the velocity strengthening behavior leads to stable sliding rather than stick-slip sliding (Marone and Scholz, 1988). Velocity strengthening has also been observed for sliding experiments on bare granite surfaces at low ($\sim 5 \text{ MPa}$) normal stress and slip rates above $\sim 10 \mu\text{m/sec}$ (Kilgore *et al.*, 1993).

The elevated b -values (e.g., Mori and Abercrombie, 1997; Gerstenberger *et al.*, 2001) sometimes reported for the upper few kilometers of faults may be a reflection of reduced frictional strength and shear stress at shallow depth.

To determine the frictional properties of the plastic material, Brune and Anooshehpour (1998) did separate tests with the entire fault covered with plastic. Under the same 330 Pa of normal stress, shear stress was measured at different sliding velocities ranging from less than 1 mm/sec up to 130 mm/sec . Sliding stress at pre-event creep velocity of 1 mm/sec was less than 100 Pa and increased monotonically to 170 Pa at 130 mm/sec sliding velocity. Measurement of the sliding stress was not possible at the typical sliding velocity of the stick-slip events (1 m/sec). By extrapolation from the values in the measured range, Brune and Anooshehpour estimated the latter shear stress value to be 230 Pa .

Numerical Model

The numerical simulations employ the method used by Day (1982). The linearized continuum equations of motion for an isotropic Kelvin–Voigt viscoelastic solid (specialized to have equal Q -values in shear and compression) are

$$\begin{aligned}\sigma_{ij} &= \rho(\alpha^2 - 2\beta^2)(u_{k,k} + \gamma\dot{u}_{k,k})\delta_{ij} \\ &\quad + \rho\beta^2(u_{i,j} + \gamma\dot{u}_{i,j} + u_{j,i} + \gamma\dot{u}_{j,i}), \\ \dot{v}_i &= \rho^{-1}\sigma_{ij,j}, \\ \dot{u}_i &= v_i,\end{aligned}$$

where σ is the stress tensor, \mathbf{u} and \mathbf{v} are displacement and velocity vectors, respectively, α and β are the P - and S -wave speeds, respectively, ρ is density, γ is a parameter proportional to the shear and bulk viscosities, and δ_{ij} is the Kronecker delta. The viscosities lead to equal shear and bulk Q -values, which decrease with frequency. These viscosities may be considered artificial, in the sense that their levels are set to selectively suppress high-frequency Fourier components of the solution that cannot be accurately computed on the grid. In practice, we set γ such that Q is of the order of 1 at the Nyquist frequency $1/2\Delta t$, where Δt is the numerical time step. These equations are solved by finite-difference approximations that are second-order accurate in space and time. Displacement \mathbf{u} is defined on the grid nodes of a 3D mesh, spatial derivatives of \mathbf{u} are defined on the cell centers, and time derivatives of \mathbf{u} (e.g., \mathbf{v}) are defined at times that leapfrog the times at which \mathbf{u} is defined. Time is stepped explicitly, which means that each updated nodal value is computed directly from the state of the model at the previous time step, independently of other updated nodal values.

A region with dimensions $4.4 \text{ m} \times 4.4 \text{ m} \times 2.8 \text{ m}$ is discretized with a nodal spacing Δx of 2 cm and a time step Δt of 0.15 msec . These numerical model dimensions are considerably larger than those of the foam model. This deliberate departure of the numerical model from the foam rubber model provides the advantage that the evolution of the wave field can be observed as it propagates away from the fault,

without the complication of the side-boundary reflections that would otherwise be present.

Faulting is formulated as a special boundary condition over a planar surface within the model, using a slip-weakening friction law (Ida, 1972). The amount of relative displacement between the fault walls (slip) is denoted s . The frictional strength of the fault is the product of normal stress σ_n and the coefficient of friction $\mu(\ell)$, which depends on the slip path length ℓ given by $\int_0^t |\dot{s}(t')| dt'$. When the magnitude of shear stress (τ) is less than the frictional strength, the slip velocity is zero and fault remains locked. Slip occurs when necessary to ensure that τ is bounded by the frictional strength, and the shear traction vector always acts in the direction opposing the slip velocity vector. For the slip-weakening model the coefficient of friction (shown in Fig. 2) is

$$\mu(\ell) = \begin{cases} \mu_s - (\mu_s - \mu_d)\ell/d_0 & \ell \leq d_0 \\ \mu_d & \ell > d_0 \end{cases}$$

where μ_s and μ_d are coefficients of static and dynamic friction, respectively, and d_0 is the slip-weakening distance. This friction law is a simplification of rate-and-state friction models (e.g. Dieterich, 1979; Ruina, 1983). The simplification entails neglect of a rate-dependent effect and has been shown to provide a good approximation to the full friction law under the high slip-rate conditions of dynamic rupture propagation (Okubo, 1989). Although the rate-dependent effects are important to earthquake nucleation, they have minimal influence on the rupture once it has begun and so can be safely ignored here. Slip-weakening friction laws of this type have been widely applied to model earthquake rupture dynamics (e.g., Ida, 1972; Andrews, 1976; Day, 1982). This type of friction law has also been found to be consistent with fault slip behavior as inferred from seismic recordings of past earthquakes (Ide and Takeo, 1997; Olsen *et al.*, 1997; Day *et al.*, 1998). Since a primary goal of this study is to validate the existing numerical modeling method, we retain this slip-weakening formulation without change rather than constructing a new fault constitutive equation that mimics specific behaviors of the scale-model experiments such as the velocity strengthening measured in the weak-zone plastic strip.

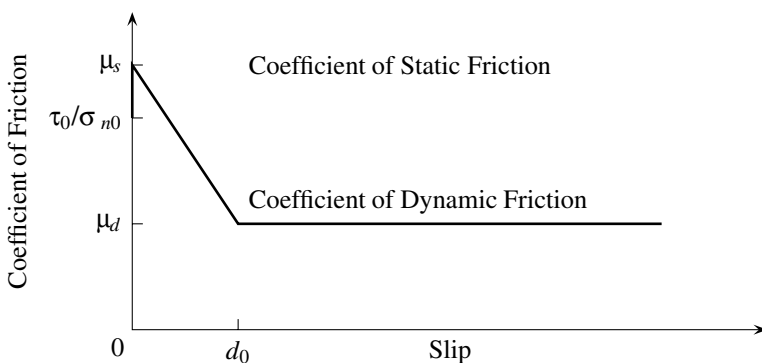


Figure 2. Behavior of the slip-weakening friction model. The curve represents the coefficient of friction at a point as a function of the cumulative path length of slip at that point.

The coefficient of static friction, μ_s , is not known for the specific foam model used in the experiments of Brune and Anooshehpour (1998). Measurements made in other foam models indicate that the coefficient depends upon normal stress but does not vary greatly among different foam models. In other experiments with normal stresses near the value of 330 Pa used in the current study, Brune and Anooshehpour (personal communication) have obtained estimates of μ_s that range from 2.3 to 3.0. We treat this quantity as a free parameter that we adjust (within that range) by trial and error to produce good agreement between the measured and simulated acceleration records on the fault. The result is a preferred value for μ_s of 2.4, which we hold fixed in all validation simulations.

Shear prestress τ_0 on the strong portion of the fault was set to the value measured by Brune and Anooshehpour (1998) in the foam experiment, 730 Pa. We set μ_d equal to the ratio of the final shear stress τ_f (610 Pa) and initial normal stress σ_{n0} (330 Pa) measurements for the physical model. This method of selecting μ_d ensures that the final shear stress in the numerical model is approximately equal to that measured in the physical model because in the numerical model the final shear stress differs little from the dynamic frictional stress.

Where foam surfaces are in contact (i.e., everywhere except in the weak zone), the slip-weakening distance d_0 was set equal to the typical size of the vesicles in the foam rubber, 1 mm (Brune *et al.*, 1990). As further support for this estimate of d_0 , Brune *et al.* (1990) note that the critical patch size (Dieterich, 1986) observed for stick slip in the foam model, ~ 10 cm, is consistent with d_0 of 1 mm.

In keeping with the approach of attempting to validate the numerical simulation method in its established form, velocity strengthening was not incorporated into the weak zone. Instead, it was roughly approximated by making the slip-weakening parameter, d_0 , infinite in the weak zone, resulting in a constant coefficient of friction there. The weak-zone friction coefficient, μ_w , was set equal to 0.6, corresponding to the Brune and Anooshehpour estimate (an extrapolation of measured values) for typical sliding velocity during a stick-slip event. Figure 3 compares the measured and extrapolated slip-rate dependence of the physical model weak-zone friction with the corresponding behavior of the

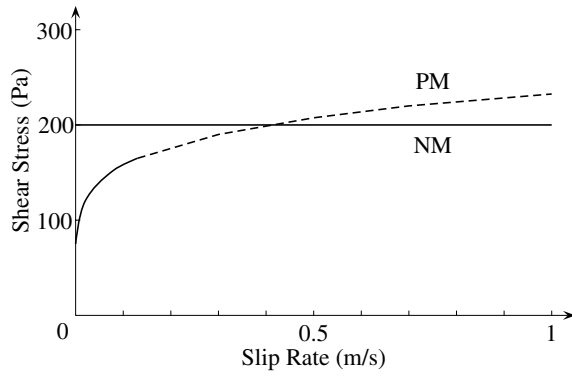


Figure 3. Frictional strength (under 330 Pa normal stress) in the weak zone, as a function of sliding velocity. The plot compares the physical model (PM) with the rate-independent numerical model formulation (NM). The solid part of the PM curve was measured in the laboratory by Anooshehpour and Brune (1998); the dashed part is their extrapolation.

numerical model. On the weak portion of the fault, the shear prestress was set to the measured value of the creep strength of the physical model weak zone, 66 Pa (see Fig. 3).

The fault ends at a depth of 1.4 m. Events are artificially nucleated at the bottom of the fault by reducing the coefficient of friction to μ_d over an expanding semicircular area. The radius of the semicircle expands at 15 m/sec until it is able to continue spontaneously, which occurs within about 40 cm of the nucleation point. Model parameters are summarized in Table 1.

We can characterize the finite-difference discretization by two important dimensionless numbers. The first is the Courant number, $\alpha\Delta t/\Delta x$, which controls stability of the time stepping. In our case, this number is ~ 0.42 , well within the stability field of our finite-difference scheme. The second important dimensionless number is $L_c/\Delta x$, in which L_c , the critical crack half-length (Andrews, 1976), serves as an estimate of the length of the slip-weakening transition zone at the rupture front. The ratio $L_c/\Delta x$ is therefore an approximation to the number of finite-difference node intervals resolving the rupture front transition. L_c is proportional to the ratio of d_0 to the strain drop, $\Delta\tau/(2\rho\beta^2)$, and for the parameters of the foam model the proportionality constant is roughly $1/2$. Therefore the rupture front transition zone is resolved by $\sim \rho\beta^2 d_0/(\Delta\tau\Delta x)$, or ~ 6 nodes.

Numerical Modeling Results

There are two goals for the numerical modeling. The first is to simulate Brune and Anooshehpour's (1998) laboratory experiments in order to validate (in the sense stated in the introduction) the numerical modeling method. The second is to use the flexibility of the numerical model to further investigate weak-zone effects.

Table 1
Numerical Model Parameters

General Parameters		
Nodes	220	220 140
Cell spacing (Δx)	2 cm	
Time step (Δt)	0.15 msec	
Damping factor (γ)	0.5 Δt	
S-wave speed (β)	30 m/sec	
P-wave speed (α)	56 m/sec	
Density (ρ)	16 kg/m ³	
Hypocentral depth	140 cm	
Weak zone depth range (h)	0–40 cm	
Fault Parameters		
	Plain Foam	Weak Zone
Initial shear stress, (τ_0)	730 Pa	66 Pa
Initial normal stress (σ_{n0})	330 Pa	330 Pa
Coefficient of dynamic friction (μ_d)	2.4	0.6
Coefficient of static friction (μ_s)	1.85	0.6
Slip weakening displacement (d_0)	1 mm	∞

Validation

For the purpose of model validation, we compare results from Brune and Anooshehpour's (1998) experiments to numerical simulation results. All parameters but one are fixed, based on the direct measurements of Brune and Anooshehpour. The exception, as discussed in the previous section, is the coefficient of static friction, μ_s , for which measurements provide us only a range of potential values. It is treated as a free parameter and is adjusted, within this permissible range, to improve the fit to the data. This μ_s value is then held fixed for all simulations in the validation study.

The data used for the comparison are acceleration records from the five near-fault, strike-parallel sensors and the fault displacement record from the surface. Because the accelerometer locations do not coincide exactly with nodes of the numerical model, nearby nodes are used for the comparison. The accelerometers are located 3 cm from the fault, while the numerical-model records are obtained at nodes 4 cm from the fault. We evaluate the acceleration data in two ways. First, we compare experimental and simulated acceleration time histories for two particular events, one with no weak zone ($h = 0$) and one with a 20-cm-wide weak zone ($h = 20$). Second, for each of a range of values of h , ranging from 0 to 30 cm, we compare simulated and experimental peak accelerations, with the latter averaged over many individual experimental events (Brune and Anooshehpour, 1998).

The numerical model is successful in reproducing many of the important aspects of the physical model acceleration records. Figure 4 shows the acceleration records for the $h = 0$ and $h = 20$ cases, using a common amplitude scale for the physical and numerical model results. The peak acceleration (PA) for each record (in units of g) is noted on the curves. We estimate apparent rupture velocities by picking the times of the maximum positive amplitudes of adjacent traces and dividing the up-dip distance by the time difference

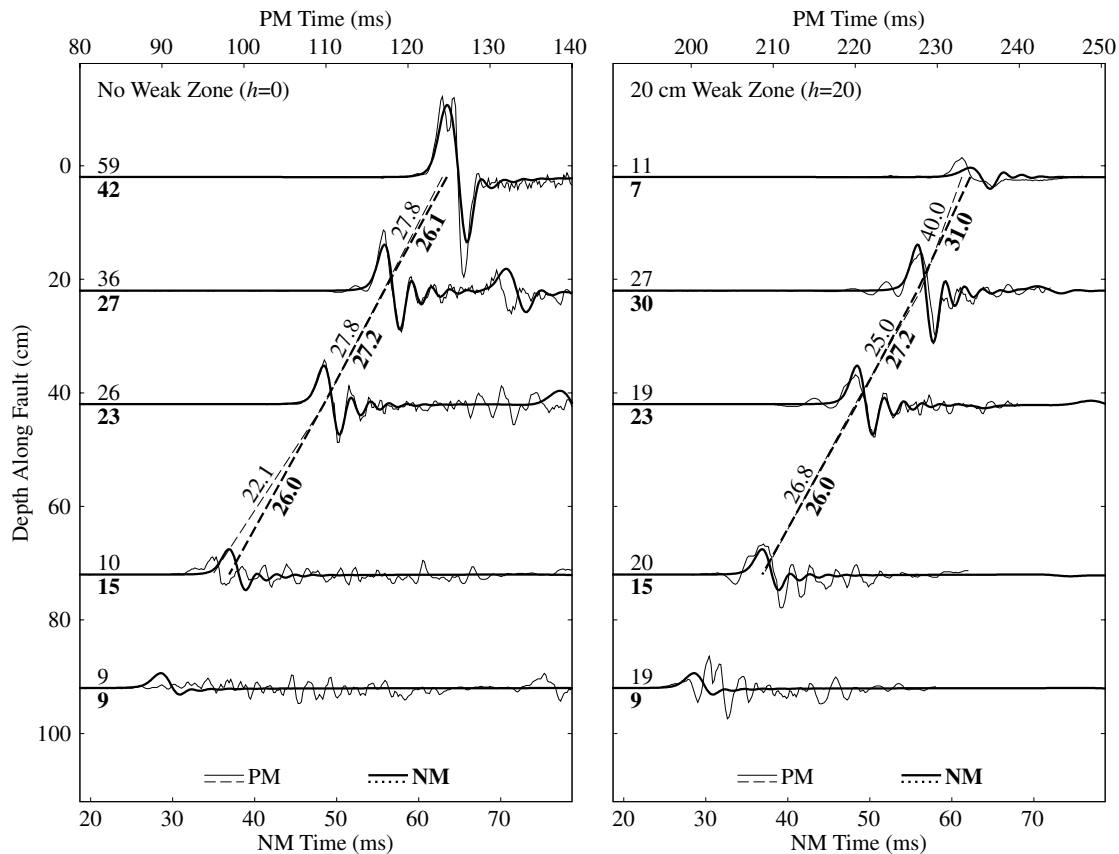


Figure 4. Comparison of physical (PM, thin curves) and numerical (NM, thick curves) model acceleration records along the fault. The case $h = 0$ (no weak zone) is on the left, and the case $h = 20$ (20-cm-deep weak zone) is on the right. All curves are plotted on a common absolute amplitude scale. Peak acceleration (in units of g) is noted at the left end of each record (light text for PM, bold for NM). Dashed lines connect times of maximum positive acceleration, and numbers on the dashed line are estimates of apparent rupture velocity (in m/sec), based on identifying rupture arrival with the time of arrival of the maximum positive acceleration pulse.

of the picks. For the physical model, this is an estimate of the apparent velocity in the up-dip direction, and if the true rupture direction is oblique to this direction, the true rupture velocity may be slightly lower than this estimate. For the numerical model this calculation approximates the true rupture velocity (except in the weak zone, as discussed later), since the hypocenter is located directly down-dip from the sensor array. Figure 4 shows the picks, connected by dashed lines, with the apparent rupture velocity noted on each line segment.

The acceleration records in Figure 4 show the strong similarities between the physical and numerical model results. A number of key features are common to both models. The main pulses are similar in shape, consisting of a positive acceleration pulse of about 4-msec duration, followed by a shorter-period negative pulse. The total duration of these strong initial acceleration phases is about 7 msec. In the absence of a weak zone, the maximum acceleration grows monotonically as the rupture progresses up-dip, and the physical model reproduces this behavior of the numerical

model. With the addition of the weak zone, both numerical and physical models show an abrupt decrease in acceleration amplitude at the near-surface station. When no weak zone is present, the main rupture pulse reflects at the surface and propagates back down the fault, producing a second, somewhat lower amplitude pulse of slip acceleration. This behavior is most evident at the sensor just below the surface sensor (second trace from the top in Fig. 4), at about 15 msec after the main pulse, and the behavior is reproduced very closely in the numerical model. Even details such as the amount of time delay between the initial phase of slip and the surface-reflected rupture phase are reasonably well reproduced (within about 10%) in the numerical simulation. When a weak zone is present in the physical model, the main pulse is suppressed as it enters the weak zone and there is no strong reflection of the rupture front. The reflection is similarly suppressed in the numerical model when the weak zone is present.

The duration of the initial positive pulse in the acceleration records (or, equivalently, the time to the peak slip

velocity) is controlled by the slip weakening parameter d_0 , and therefore the agreement in pulse duration between numerical and foam rubber models shown in Figure 4 constitutes further evidence that we have correctly estimated d_0 for the foam model. To clarify the association between pulse durations in Figure 4 and the slip weakening parameter, recall that we previously estimated the rupture-front transition length in the foam model to be roughly $\rho\beta^2 d_0/\Delta\tau$. Assuming $d_0 = \sim 1$ mm, this relationship implies a rupture front transition length of ~ 12 cm. Dividing this value by the observed rupture velocity of ~ 28 m/sec gives a duration of ~ 4 msec for the slip-weakening transition, which is very close to the duration of the initial positive acceleration pulses in Figure 4.

The estimates of apparent rupture velocity, in both physical and numerical models, are mostly in the range 27 ± 1 m/sec, which is slightly slower than (about 90% of) the S -wave velocity of 30 m/sec. Two things are remarkable about the apparent rupture velocities in Figure 4. The first is that the numerical and physical models agree so closely in their quantitative predictions. For the case of no weak zone, for example, the average rupture velocities in the two models are virtually indistinguishable. The second is that the effect of introducing the weak zone is qualitatively and quantitatively very similar in the numerical and physical models. When the rupture enters the weak zone, the apparent up-dip velocity increases to above 30 m/sec. This effect is present in both physical and numerical models, being more pronounced in the physical model.

The occurrence of apparent rupture velocity above the S -wave speed of 30 m/sec as the rupture enters the weak zone requires further comment. Normally, the S -wave speed is considered the physical limit on the rupture velocity in mode III crack extension (e.g., Broberg, 1999, p. 36), the mode which predominates here in the up-dip direction. One complicating consideration is that the rupture velocities for the physical model are apparent velocities in the up-dip direction, and if the true rupture direction is oblique to this direction the apparent up-dip velocity that may be slightly higher than the true rupture velocities. However, the high velocity occurs only when the weak zone is added to the model, localized at the weak zone, and present in the numerical model as well (where it is known that the actual rupture direction is up-dip). Therefore, the high apparent rupture velocity is almost certainly not a simple geometrical artifact due to an oblique rupture direction. A velocity in the weak zone exceeding the S speed would not be physically precluded in this case. Since the rupture on the strong part of the fault travels slower than the S -wave speed, the S waves from that part of the fault arrive in the weak zone ahead of the rupture front, and they could trigger early rupture within the weak zone.

However, a careful analysis exploiting the detailed wave-field images available from the numerical solutions leads to a different conclusion. In the case of the numerical model, the appearance that rupture velocity is high in the

weak zone results from the slight offset of the acceleration sensors from the fault plane (to correspond to the sensor locations in the foam rubber experiments). The true rupture velocity in the weak zone of the numerical model (as measured directly on the fault plane) is actually relatively low, and this is probably the case in the foam rubber model as well. That analysis is presented in detail in the next section.

Acceleration amplitudes in the physical and numerical models can be compared quantitatively, although some caution is called for. Near the fault, acceleration falls off rapidly with distance from the fault, causing the amplitude of the acceleration records to be highly sensitive to sensor location. As previously noted, the node locations in the numerical model are not exactly coincident with the sensor locations of the physical model, introducing some degree of ambiguity in the amplitude comparison between the two models. Also, event magnitude and hypocenter location are variable in the foam rubber model and are not known for the two particular events for which we have examined the acceleration time histories. To minimize these variations, Brune and Anooshehpour (1998) looked at normalized PA averaged over many events. Their normalized values are the ratio of PA relative to a reference point at depth. The event averaging offers a consistent comparison with the numerical model results, in the sense that the numerical model parameters τ_0 and μ_d were determined from initial and final stress values for the foam rubber model that were themselves averages over many events.

Figure 5 shows normalized PA curves for both the physical model (dots, from Brune and Anooshehpour [1998]) and the numerical model (solid curves). The reference point is at 56 cm depth, which is well below any weak-zone effects. In addition to the two model events, $h = 0$ and $h = 20$, the PA curves also include data for weak-zone thicknesses of $h = 7.5, 15,$ and 30 cm. The numerical model normalized PA curves show that, for $h = 0$, the amplitude also varies rapidly with depth near the rupture break out at the free surface. Therefore the physical model amplitude at the near-surface sensor is probably also highly sensitive to sensor depth, as well as distance from the fault, and possibly even affected by the finite size of the sensors. Figure 5 shows significant similarities between the model results. In both models the PA at the surface is reduced by the presence of the weak zone, and the wider the weak zone the greater the reduction factor. At the near-surface sensor, for the no-weak-zone case ($h = 0$), the normalized PA is 2.5 for the physical model and 1.9 for the numerical model, a 25% difference. For $h = 20$ the normalized PA at the surface is 0.44 for the physical model and 0.31 for the numerical model, a 29% difference.

Figure 6 compares measurements from the displacement sensor located on the fault trace at the position shown in Figure 1. The sensor measures half of the total slip on the fault. Measurements by Brune and Anooshehpour (1998) are shown by the thin curves, and the numerical model results are shown by the thick curves. The left panel shows the no-

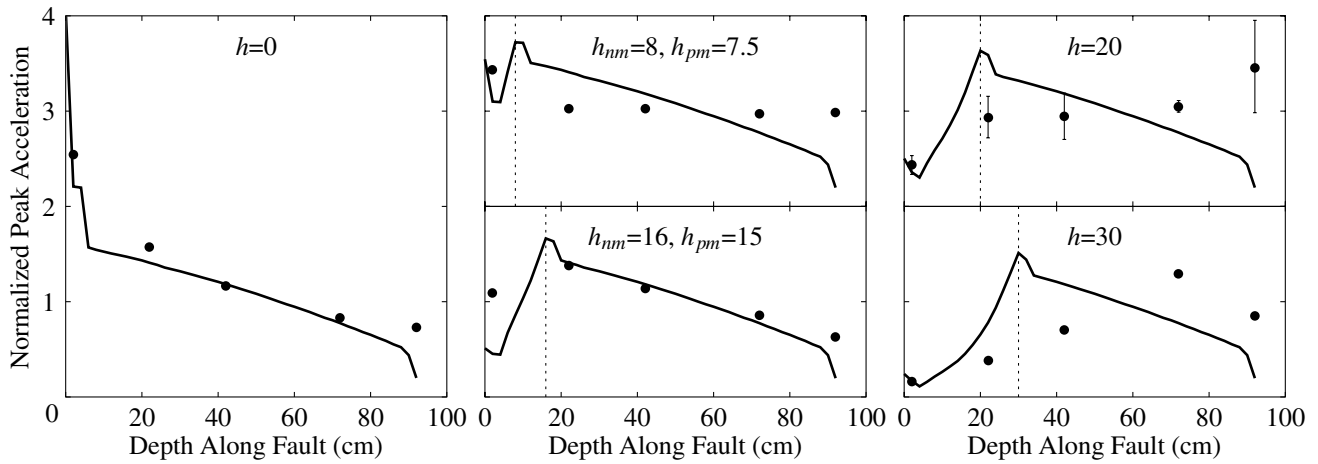


Figure 5. Normalized peak acceleration on fault. Values for the physical model are normalized to the value halfway between the sensors at 40 and 70 cm depth and are also averaged over many experimental events. Numerical model curves are normalized to the computed value at 56-cm depth. The subplots are labeled by the weak-zone thickness, h , in cm. In cases where the numerical model had a slightly different weak-zone thickness than the physical model (due to the spatial discretization of the former), the thicknesses are denoted by h_{nm} and h_{pm} , respectively.

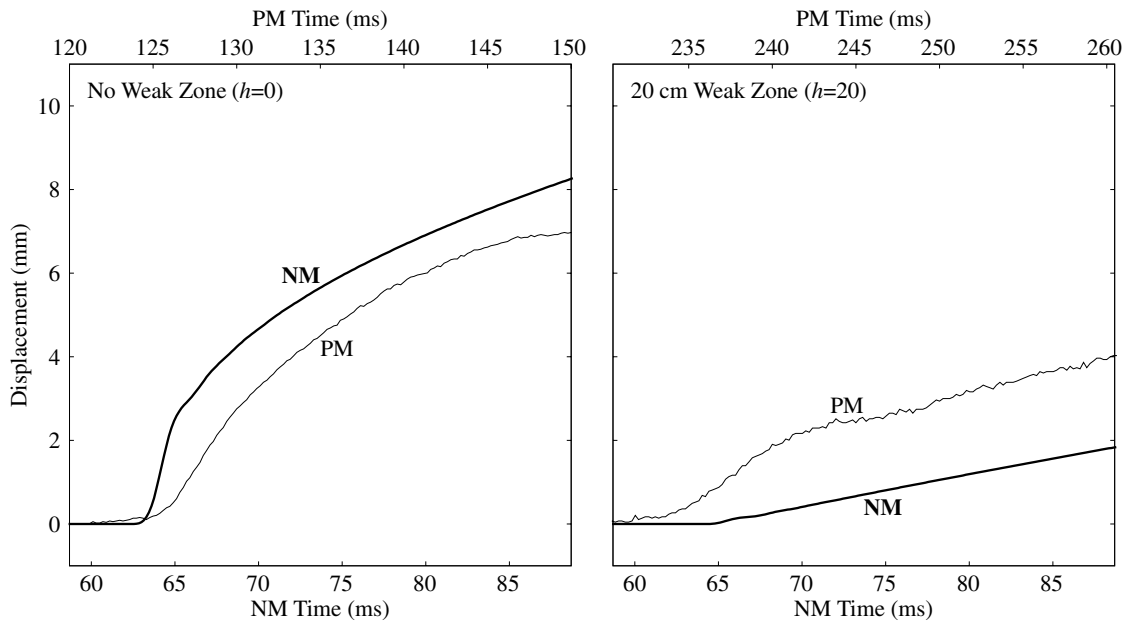


Figure 6. Displacement (half the slip) at the surface sensor (see Fig. 1 for displacement transducer location). Measurements for the foam rubber physical model (PM) are shown by the thin line, calculated record for the numerical model (NM) simulation by the thick line. The left panel shows the case of no weak zone ($h = 0$), and the right panel shows the 20-cm weak-zone case ($h = 20$).

weak-zone case ($h = 0$), and the right panel shows the 20 cm weak-zone case ($h = 20$). The two models are in good agreement for the no-weak-zone case. For the 20-cm weak-zone case, the numerical model underpredicts slip. In a subsequent section, we show that the latter result is sensitive to the friction μ_w in the weak zone and that the results can

be brought into close agreement with a modest adjustment of μ_w .

Note, comparing the slip duration (Fig. 6) with the total rupture time (Fig. 4), that the slip behavior is cracklike, not pulslike, in the sense that the duration of slip is comparable to the total duration of the event. The cracklike behavior,

combined with the degree of agreement between numerical and physical model results, strongly supports our claim that fault offset in the foam rubber model occurs predominantly through frictional sliding, rather than through frictionless shear movement during a fault opening episode at the rupture front.

Further Analysis of the Numerical Simulations

An advantage of the numerical model is that each node in the finite-difference discretization is, in effect, a sensor, providing a high-resolution record of motion for the entire model. One can use the high resolution provided by the numerical solution to learn more about the dynamics of the fault model. In the acceleration records (Fig. 4) the rupture propagates from below up to the surface. It appears in both the physical and the numerical model as though the velocity of the rupture increases when it enters the weak zone. We use the high-resolution wave-field information from the numerical model to look at this effect more closely.

Figure 7 shows synthetic acceleration records, at the resolution of the numerical model, for the upper 40 cm of the fault. The two top panels (Fig. 7 a,b,) show vertical record sections that are located 4 cm from the fault, for $h = 0$ and $h = 20$, respectively. These are more-detailed views of the same profile that is shown in Figure 4, and we note again that rupture apparently speeds up as it enters the weak zone. The two bottom panels (Fig. 7 c,d) show what happens at the nodes directly on the fault (points not sampled in the foam experiments). Each curve is normalized by its PA, which is noted (in g) on each curve. The larger accelerations for the profile at the fault illustrate how rapidly acceleration decreases with distance from the fault. In contrast to the near-fault records, the on-fault records show that the rupture actually slows down in the weak zone. The apparent increase in rupture velocity recorded near the fault merely reflects the fact that when rupture dies out, a strong S -wave pulse continues to travel up-dip and is observed at the sensor locations 3 cm (4 cm in the numerical model) off the fault plane.

This effect can also be seen in Figures 8 and 9, which show snapshots of particle velocity on a cross section of the fault through the hypocenter. Figure 8 shows the $h = 0$, case and Figure 9 shows the $h = 20$ case. The fault vertically bisects each image. The color indicates the strike-parallel component of velocity (particle motion is normal to the plane of the cross section). Since the cross section is the plane of symmetry for the bilateral rupture, the motion is purely strike parallel. For the $h = 20$ sequence, the rupture enters the weak zone at the 58.5-msec frame, and particle velocity on the fault begins to decrease. By 61.5 msec, the rupture has clearly slowed while the S -wave pulse remains strong a few centimeters from the fault. The unbroken part of the fault can be seen as a narrow white strip in the top 20 cm of the model in the 61.5 ms panel of Figure 9. This unbroken strip then gradually narrows as the rupture continues to the surface between 61.5 msec and 66 msec. When the weak zone ruptures, there is no local release of strain

energy to offset the frictional work done. Therefore, the rupture front is weakened, and no strong reflected front is evident following the surface breakout (at about 66 msec) in Figure 9. In comparison, the no-weak-zone ($h = 0$) simulation in Figure 8 has a very strong reflected rupture front that propagates back down the fault beginning at about 64.5 msec.

We now turn our attention to motion at the ground surface of the model. Surface motion was not recorded for the physical model (apart from the single displacement record at the fault plane) but is of course available from the simulations at the 2 cm node spacing of the numerical model. Figure 10a and b, respectively, shows surface profiles of PA and peak velocity (PV) (strike-parallel component) for numerical simulations with a range of weak-zone thicknesses. The profiles are perpendicular to the fault on a line through the epicenter, and they extend 80 cm away from the fault on the model ground surface. The uppermost curve is the $h = 0$ case, and successively lower curves are for weak-zone thicknesses increasing in 4-cm increments. The bottom curve is the $h = 40$ case. When no weak zone is present, or when the weak zone is shallow, both PA and PV diminish rapidly with distance from the fault. In these cases, PA diminishes away from the fault much more quickly than PV. Both PA and PV are greatly reduced near the fault as h increases. In fact, for very deep weak zones, PA and PV are smaller at the fault than they are some distance away.

In order to highlight the weak-zone effects, we look at the ratios of PA and PV relative to the case with no weak zone. Figure 11 shows the ratio of PA (a) and PV (b) to corresponding values for no weak zone, as a function of distance from the fault. With results plotted in this form, it is clear that the lateral distance from the fault over which the weak zone diminishes PA and PV increases with weak-zone thickness. For example, for $h = 20$, PA is reduced for all distances inside 14 cm, and for $h = 40$, PA is reduced inside 27 cm. Outside the zone of decreased PA lies a zone in which PA is increased by almost a factor of 2 in the presence of a weak zone, relative to the case with no weak zone. PV decreased everywhere relative to the no-weak-zone case, but the region of highest reduction is near the fault, and this region widens with weak-zone depth. The zone of increased PA is a somewhat surprising prediction of the numerical model, and we have no measurements in the foam model with which to compare it. We can get some understanding of the origin of this effect by examining the cross-section snapshots of particle velocity shown in Figure 9. The snapshots reveal that when rupture enters the weak zone, a new wavefront radiates from the point of entry. Beginning at 60 msec, just after the rupture has entered the weak zone, this phase appears as a widening circle of low particle velocity. This phase is akin to the stopping phase that is excited when crack growth terminates abruptly. In the present case, however, the phase is associated with rupture deceleration and abrupt reduction in dynamic stress drop at the base of the weak zone. At 66 msec, this deceleration phase begins to

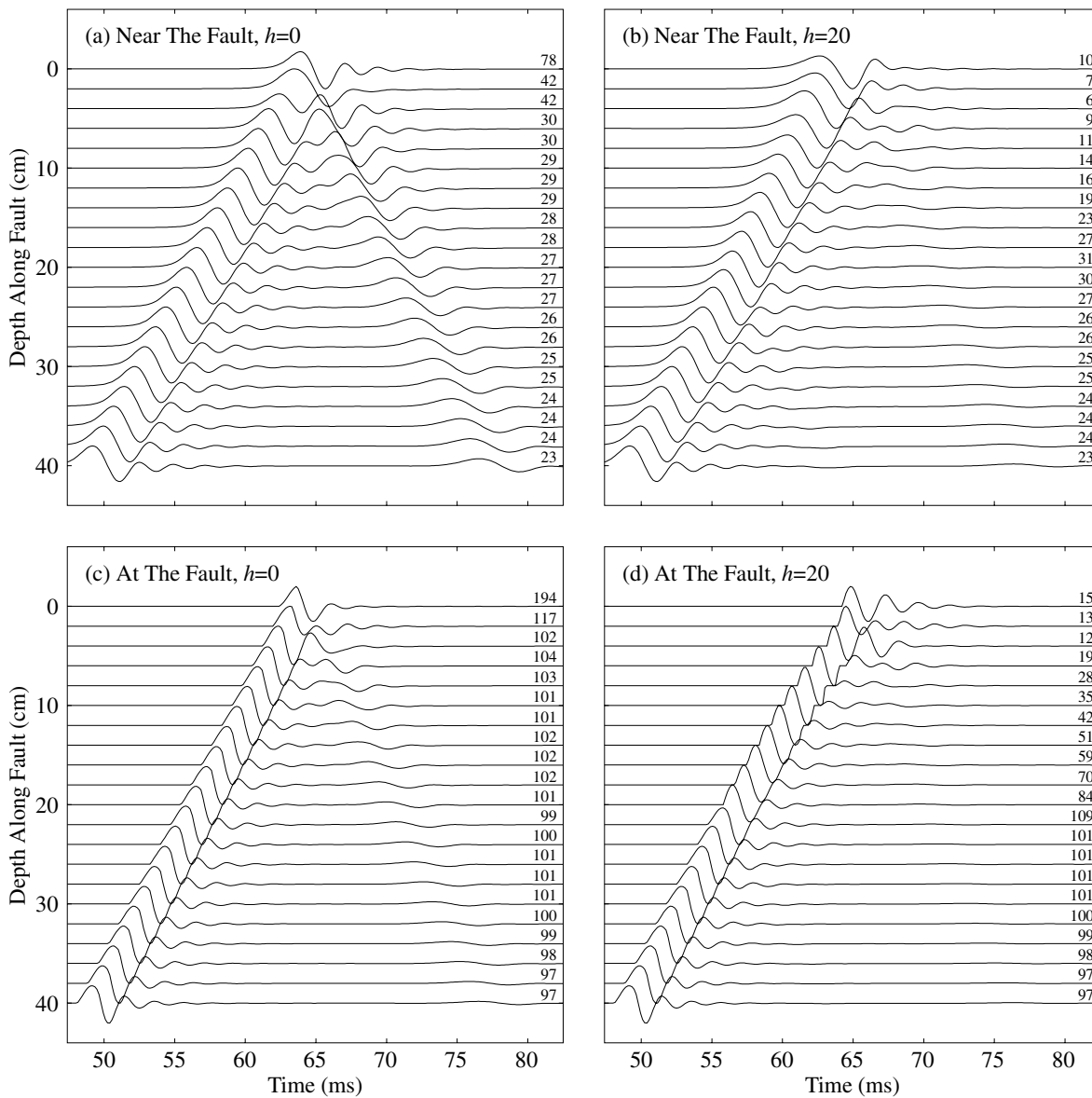


Figure 7. Comparison of numerical model acceleration records near the fault (panels a and b, for $h = 0$ and $h = 20$, respectively) with corresponding records at the fault (panels c and d). Each trace is separately scaled, the number on each curve indicating peak acceleration (in units of g).

reflect at the free surface, and the intersection of the phase front with the free surface propagates horizontally away from the fault. At the phase front is a relatively abrupt reduction in particle velocity that leads to the elevated (relative to $h = 0$ case) accelerations that occur beginning at distances of order h from the fault.

Sensitivities

In this section, we describe some additional simulations that indicate the sensitivity of the numerical simulations to variations in two model parameters, the static coefficient of friction of the foam rubber (μ_s), and the coefficient of friction of the weak-zone material (μ_w), respectively. We single out

these two parameters because their experimental values have relatively high uncertainties. In the case of the former, we have a range of estimated values of μ_s for similar foam models, but none for the model used in the experiments studied here. In the case of the latter, direct measurements (as opposed to extrapolation) are only available over a small portion of the range of relevant slip velocities (Fig. 3). Our additional simulations use modified values of μ_s and μ_w , but the selected values remain within the ranges consistent with the available measurements.

Figure 12 compares the experimental acceleration records for $h = 0$ (no weak zone) and $h = 20$ cm, respectively, with a corresponding pair of numerical simulations with a

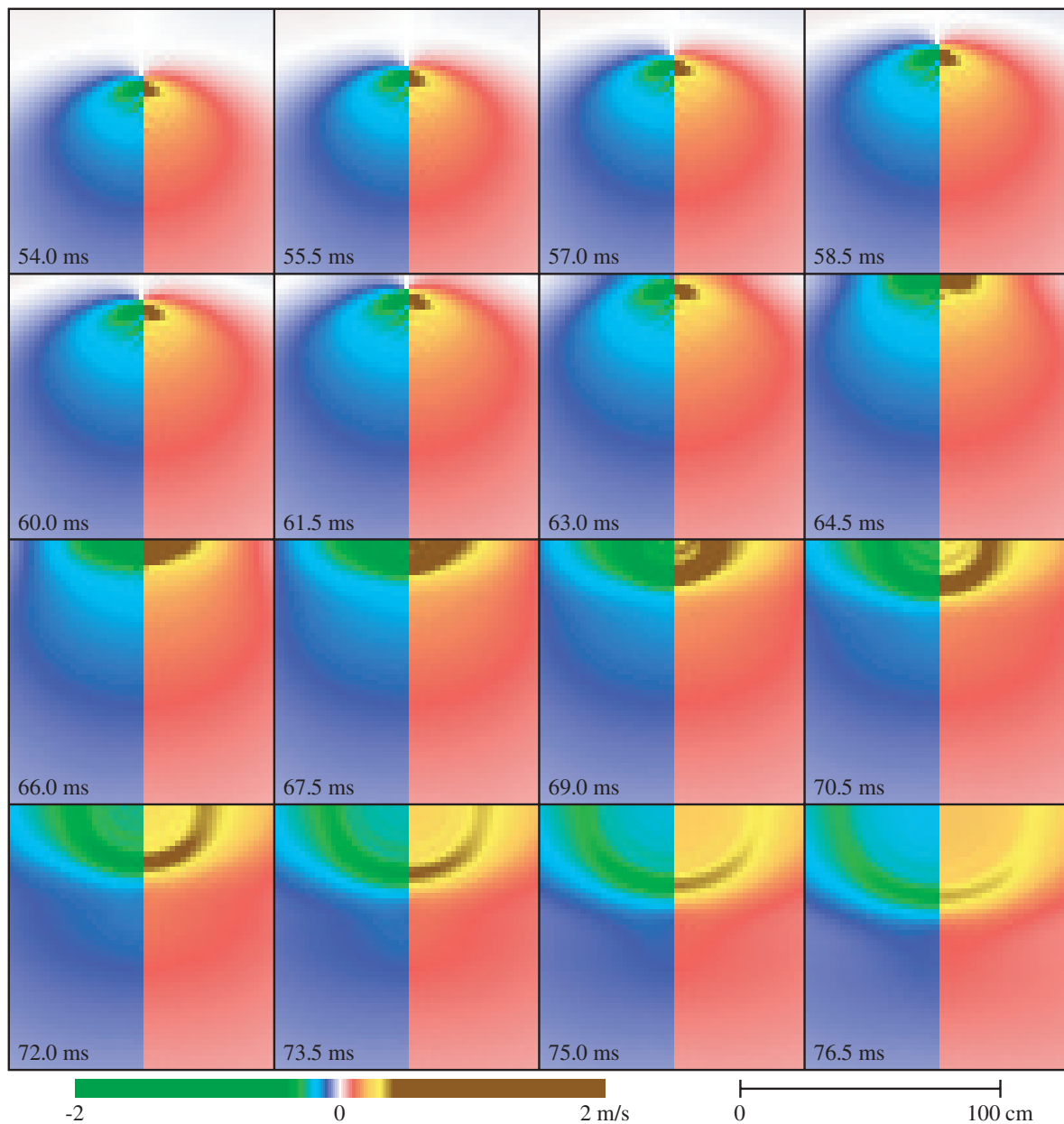


Figure 8. Cross-sectional snapshot images of the along-strike component of particle velocity for the case with no weak zone ($h = 0$). The fault bisects each snapshot, and particle motion is normal to the plane of the cross section.

modified μ_s . In both cases, μ_s has been reduced from our preferred value of 2.4 to a value of 2.3. This change cuts in half the difference $|\mu_s \sigma_{n0} - \tau_0|$ between the shear prestress and failure stress in the numerical model. In comparison with results for the preferred model in Figure 4, the reduction of μ_s results in slightly increased PAs and rupture velocities at most sensor locations. The surface slip, shown in Figure 13, increases by about 10%–20% in the modified model, bringing the $h = 20$ case somewhat closer to the experimental results, while moving the $h = 0$ case a little further away from the experimental results. The quality of agreement of experiment and simulation is not significantly different with

the two values of μ_s . However, the comparison is significant in that it shows that reduction of μ_s , because it reduces the energy dissipation near the rupture front, increases slip acceleration amplitudes and rupture velocities.

The velocity-dependent coefficient of friction in the weak zone, μ_w , was measured by Brune and Anooshehpour (1998) over the range ~ 1 to ~ 120 mm/sec. Their estimates of μ_w at velocities characteristic of slip during the model earthquakes (of order 1 m/sec) required extrapolation over a one order of magnitude range in slip velocity. The directly measured values of μ_w range from ~ 0.24 to ~ 0.5 , and the extrapolated value at 1 m/sec is ~ 0.7 . Compounding the

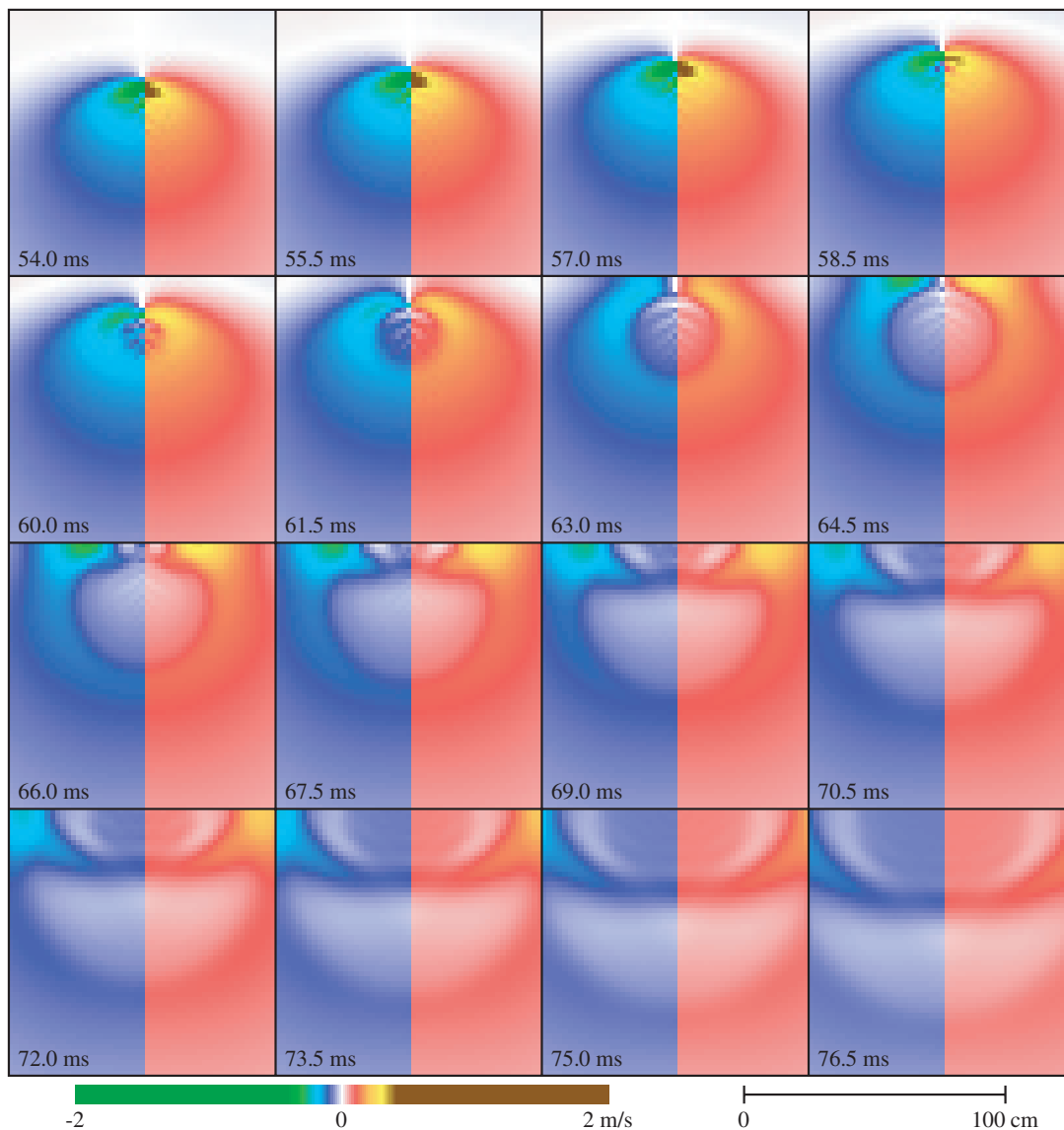


Figure 9. Cross-sectional snapshot images of along-strike particle velocity for the case with a 20-cm weak zone.

uncertainty, our numerical model neglects the velocity dependence and uses a fixed coefficient of friction (i.e., infinite d_0) in the weak zone. While our original value for μ_w of 0.6 was chosen near the center of the range of inferred (measured plus extrapolated) experimental values (see Fig. 3), there is no certainty that this single value will yield dynamic behavior representative of the actual velocity-strengthening model, even assuming the extrapolation is reliable.

We find that varying μ_w within the range suggested by the experiments has a relatively small effect on the simulated acceleration records, but a rather large effect on the surface slip. Figure 14 shows the acceleration records for the $h = 20$ case (again compared with the experimental results) when μ_w is reduced to 0.4, which is near the center of the range of directly measured values (corresponding to slip velocity of ~ 30 mm/sec). Other constants are the same as in the

original model (Table 1). The case $h = 0$ is shown again for comparison purposes, but since μ_w only affects the weak zone, this case is unchanged from the original $\mu_w = 0.6$ simulation shown in Figure 4. In the $h = 20$ case, the accelerations are still nearly unchanged relative to the original model by the reduction in μ_w , except at the uppermost sensor, which lies within the weak zone. There the PA is increased and in better agreement with the experiment. The reflected rupture phase present on the second trace down is now more prominent than in the original model, while this phase is not visible in the experimental record. Table 2 summarizes PA results at the surface sensor from simulations with a range of weak zone depths h . In each case, results for each of the two μ_w values are shown and compared with the corresponding experimental values. The lower μ_w case shows better overall agreement with the physical model than

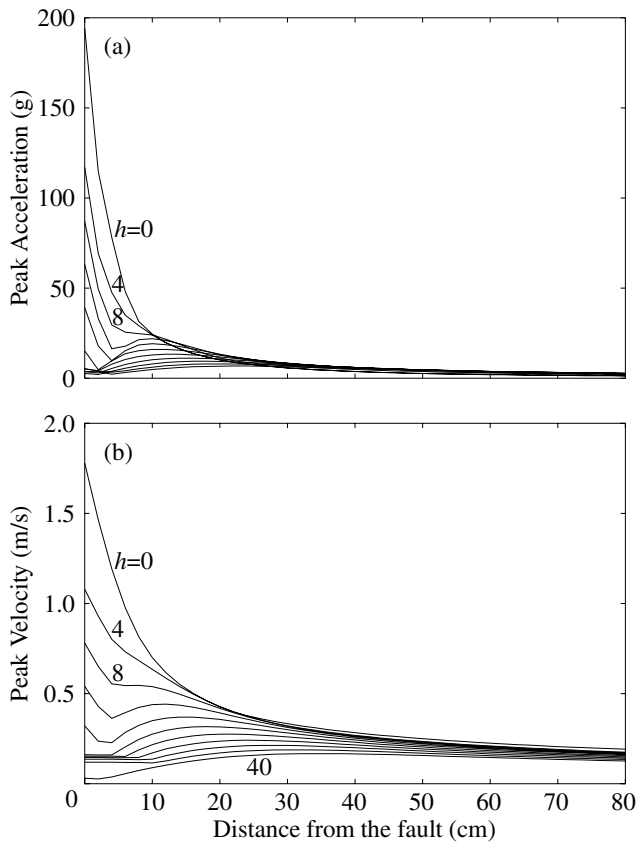


Figure 10. (a) Peak acceleration and (b) peak velocity computed at the surface of the numerical model. The profiles are perpendicular to the fault on a line through the epicenter. The curves represent different weak-zone depths (h) ranging from 0 to 40 cm.

does the higher μ_w case. The lower μ_w simulations overestimate surface PA for large h and underestimate it for small h , while the higher μ_w simulations underestimate surface PA for all h . Figure 15 shows the surface slip for the $\mu_w = 0.4$ simulation. The reduction of weak-zone friction increases the slip by nearly a factor of 2, greatly improving the agreement with experiment in this respect.

We can gain further understanding of these effects of reducing μ_w from the cross-section snapshots of particle velocity for the $\mu_w = 0.4$, $h = 20$ simulation, shown in Figure 16. At 61.5 msec, the velocity of the rupture front and the associated particle velocities are not as sharply reduced when they encounter the weak zone as was the case in the original model ($\mu_w = 0.6$, $h = 20$; Fig. 9). In the $\mu_w = 0.4$ case, the rupture front retains sufficient energy to reflect off the free surface (64.5 msec) and send a second acceleration pulse back down the fault. In the original ($\mu_w = 0.6$) simulation, in contrast, the higher strength of the weak zone caused it to damp the rupture and suppress the rupture reflection, greatly reducing the total slip.

On balance, reduction of μ_w appears to improve the agreement of the numerical simulations with experiment. Both surface PA values and total slip values are in better

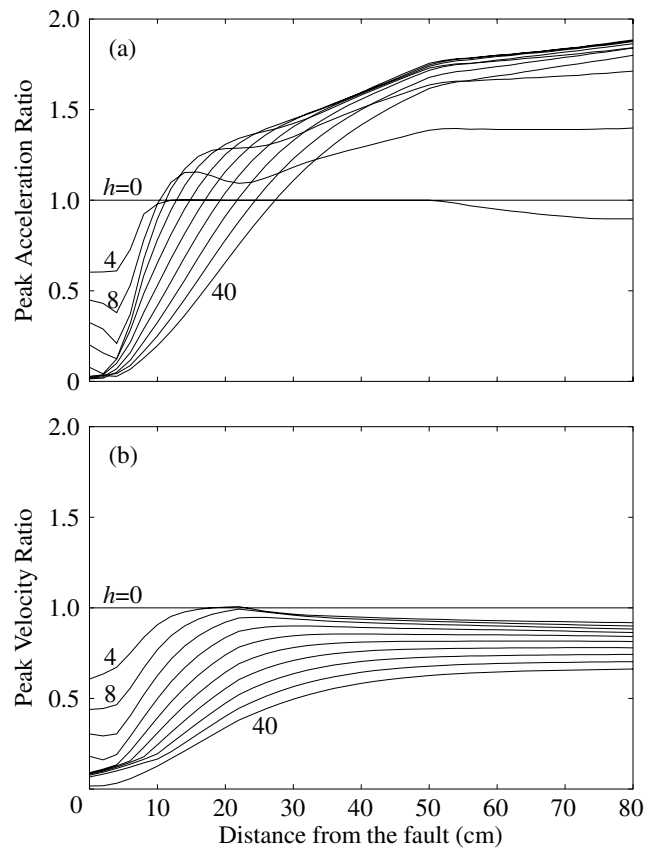


Figure 11. Same as Figure 10, but displayed as ratios of (a) peak acceleration and (b) peak velocity values to the case with no weak zone.

agreement with $\mu_w = 0.4$. Some discrepancies remain. It does not appear that adjustment of μ_w alone can bring the surface peak acceleration values into precise agreement for all h . In addition, the lower value of μ_w that improves the prediction of the total slip also predicts a very distinct reflected rupture phase at the second sensor that is not observed experimentally. It is likely that the numerical model behavior could be brought into even better agreement with experiment by incorporating the observed velocity-strengthening into the numerical model weak-zone friction law.

Discussion

The scale-model earthquake experiments challenge numerical simulations in ways that real earthquake data cannot. Firstly, the experiments sample the wave field very close to the fault, and at multiple depth points, which is not feasible for natural earthquakes. Secondly, the relevant bulk and fault-surface properties of the foam and plastic weakening strip, as well as the initial and final stress states, are known with far more completeness and far greater precision than are the corresponding properties and stress states of natural fault zones. The resulting constraints leave very little freedom for adjusting the parameters of the numerical model

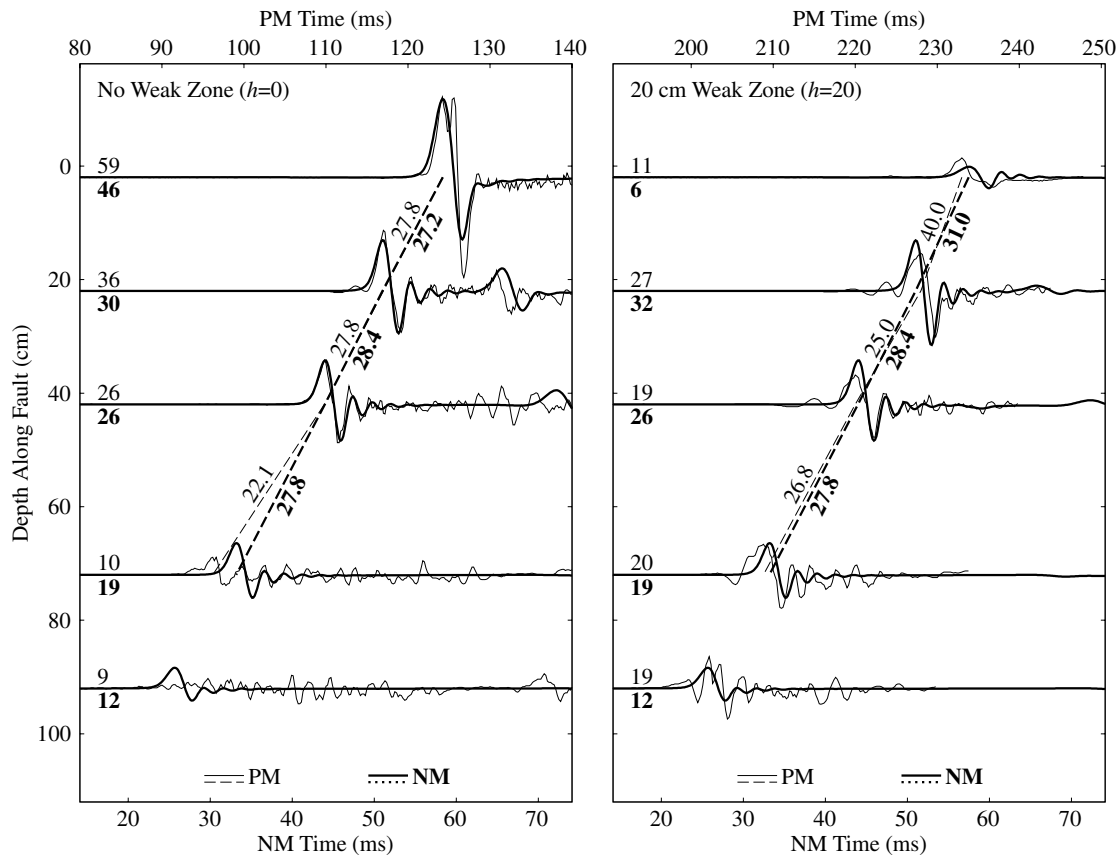


Figure 12. Comparison of physical (PM, thin curves) and numerical (NM, thick curves) model acceleration records along the fault for simulation with modified μ_s value (2.3). Other model parameters are as in Table 1. Annotations are the same as in Figure 4.

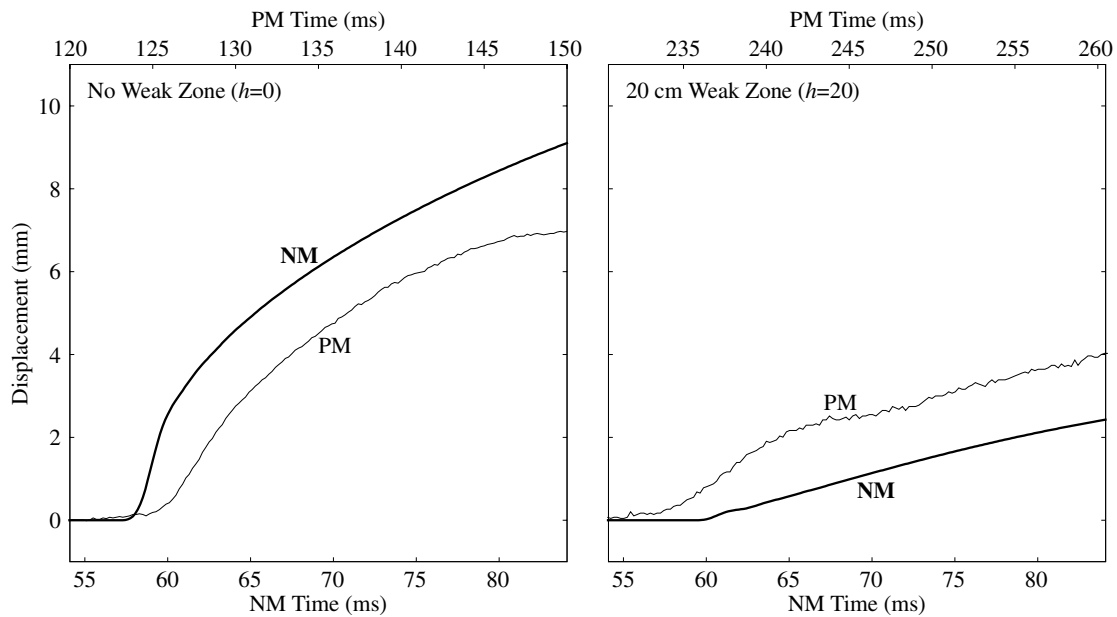


Figure 13. Displacement (half the slip) at the surface sensor for simulation with modified μ_s value (2.3). Figure annotations follow Figure 6.

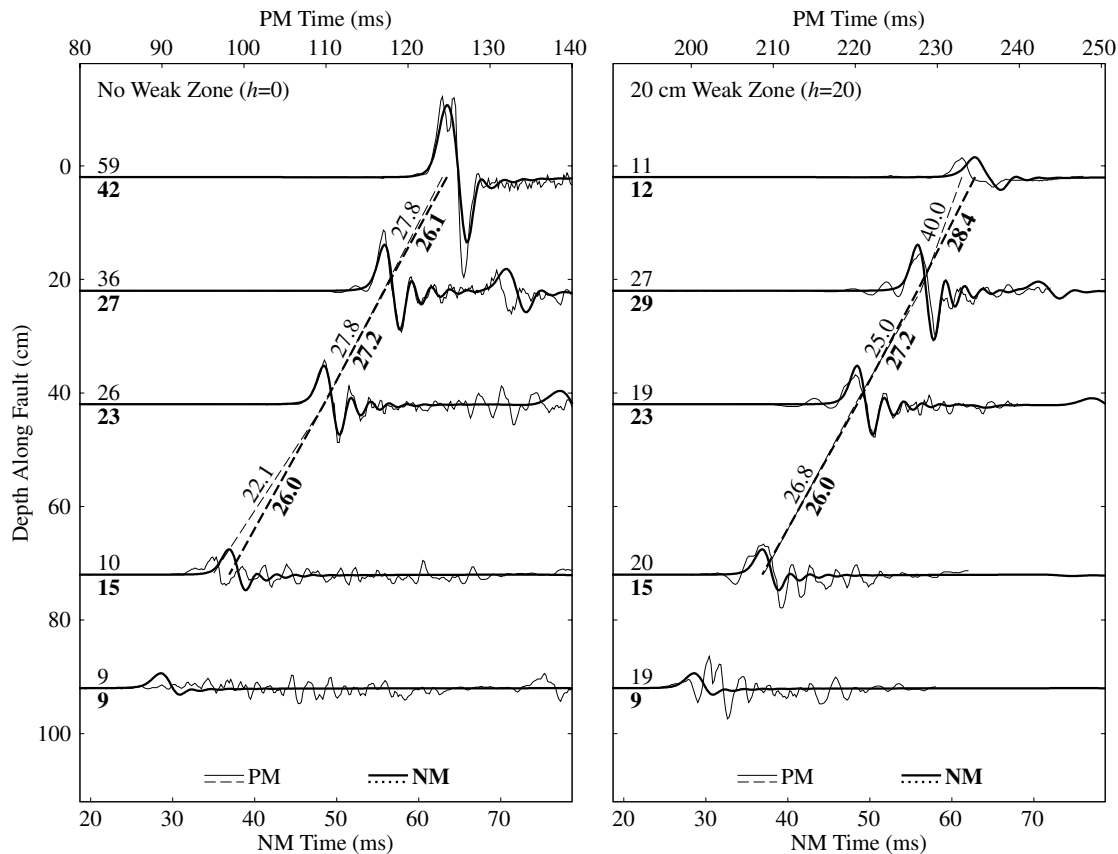


Figure 14. Comparison of physical (PM, thin curves) and numerical (NM, thick curves) model acceleration records along the fault for simulation with modified μ_w value (0.4). Other model parameters are as in Table 1. Annotations are the same as in Figure 4.

Table 2
Normalized Surface Peak Accelerations

	Weak Zone Thickness, h (cm)				
	0	7.5 (8)	15 (16)	20	30
Physical model	2.54	1.44	1.09	0.44	0.16
Numerical model ($\mu_w = 0.6$)	1.91	0.95	0.39	0.31	0.15
Numerical model ($\mu_w = 0.4$)	1.91	1.24	0.71	0.53	0.20

Numerical model weak zone depth is shown in parentheses when it differs from physical model value.

and therefore add considerably to the significance of achieving close agreement between simulations and experimental records. Thirdly, the experiments can be repeated with a given model parameter varied while all others are held fixed. The numerical simulations may therefore be evaluated not only with respect to their ability to match an individual experiment, but also with respect to their ability to match the quantitative changes that occur as a parameter (such as weak-zone depth h) is varied.

Our numerical simulations exploited all of these attributes of the scale-model experiments. The only model pa-

rameter adjusted in the validation study was μ_s . That parameter was adjusted only within the range permitted by experimental constraints, and then it was held fixed when weak-zone depth h was varied. Further numerical experiments with variations in μ_w were also done only within the constraints permitted by experimental measurements. We would claim, therefore, that the comparisons presented here provide an unprecedented level of validation for a numerical earthquake-simulation methodology.

Though we established a preferred value of μ_s for the numerical model by optimizing the agreement of numerical and experimental acceleration pulses, we caution that this value may not necessarily be a good estimate for the actual μ_s of the foam rubber. Since this is the only numerical model parameter adjusted during the validation study, it must accommodate any discrepancies in the underlying physics of the two models. For example, there remains the possibility that the foam rubber fault might open briefly at the rupture front (Brune *et al.*, 1993), in which case the foam model would have a greater dynamic stress drop than the numerical model during the first few milliseconds of shear displacement. Such behavior could result in the foam rubber model generating stronger slip accelerations than would be the case

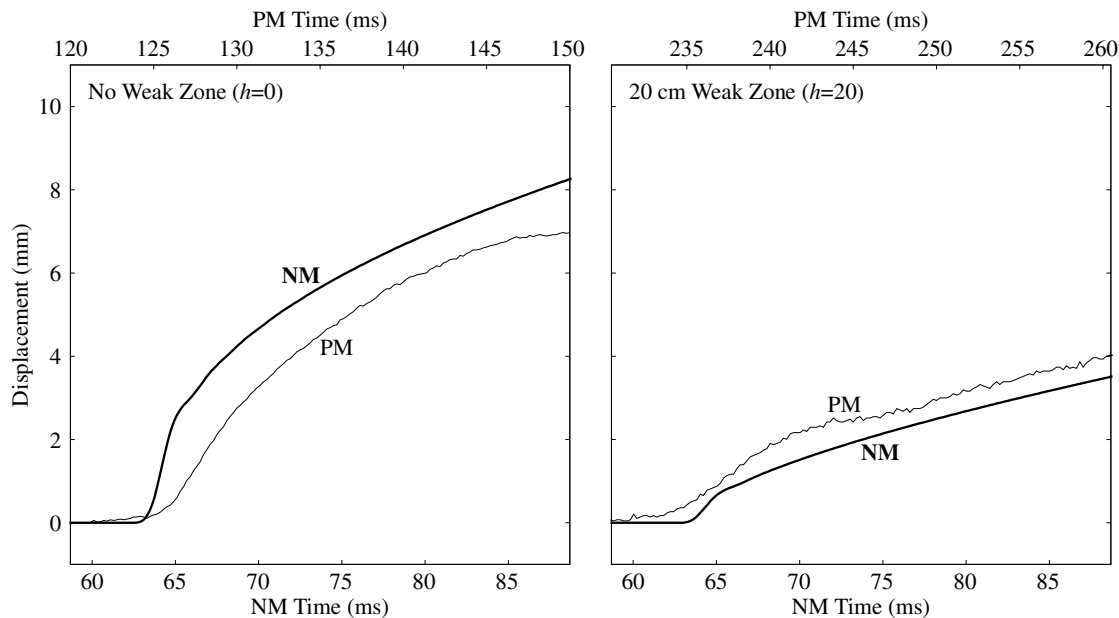


Figure 15. Displacement (half the slip) at the surface sensor for simulation with modified μ_w value (0.4). Figure annotations follow Figure 6.

with the friction law used in the numerical model. Under that hypothesis, the value selected for μ_s in the numerical model might be lower than its actual value in the foam, in order to compensate for the momentarily lower dynamic stress drop of the numerical model just behind the rupture front. As noted previously, calculations confirm that lower μ_s has the effect of increasing rupture velocity and rupture-front accelerations in the numerical simulations. Put differently, it is possible that μ_s is simply serving as a parameter that permits us to equalize the energy dissipation near the rupture front in the two models.

While the experimental validation study does not demonstrate relevance to natural earthquakes, it fills an important gap in our understanding of numerical models for earthquake dynamics. At the most basic level, of course, the simulations of the laboratory experiments provide strong evidence that the simulation code is free of major programming errors. At this level, however, validation could reasonably have been achieved by comparison with independently programmed simulation methods. Also, the various elements of the code (e.g., the elastodynamic equations governing the bulk behavior, the free-surface boundary condition, the fault frictional behavior) had, of course, already been thoroughly tested individually by simulating a series of idealized linear problems for which analytical solutions exist. So, while achieving agreement with a physical model is a satisfying demonstration of the integrity of the coding logic, this is not the most significant aspect of the problem.

More significant is that we have obtained an independent confirmation of the inherent adequacy of the discrete approximation of the continuum used in the numerical model. The experimental confirmation is significant because

the problem of spontaneous rupture propagation and frictional sliding is highly nonlinear. The nonlinearity arises principally from the fact that rupture evolution and arrest are determined as part of the dynamic solution, not given as part of the *a priori* problem specification. In other words, we have a mixed boundary value problem in which the respective (time-dependent) domains of displacement and traction boundary conditions are themselves dependent upon the displacement and stress fields. There are no analytical solutions describing the complete fault motion and wave field for problems of this class, nor are there any general mathematical proofs of convergence for the equations governing discrete approximations to the system. We are left with no obvious alternatives to the experimental approach to validating the discrete approximations.

One specific way in which the nonlinearity manifests itself is in the phenomenon of length-scale collapse. We expect, on the basis of asymptotic analysis (e.g., Freund, 1990, chapter 4), that the velocity field near the rupture front will Lorentz contract (in the direction of rupture propagation) as the rupture accelerates toward its limiting speed (e.g., the *S*- or Rayleigh-wave speed). This contraction of length scale in the spontaneous rupture problem inevitably transfers energy to progressively higher wavenumbers, a process that is artificially truncated at the Nyquist wavenumber of the numerical grid. We use a scale-selective damping (described previously) to prevent accumulation of energy near the grid Nyquist wavenumber, an approach similar to that commonly used to stabilize shock-wave calculations. The implicit assumption is that the viscous damping takes the place of unmodeled, nonlinear dissipative processes that limit scale contraction in the actual physical problem. The experimental

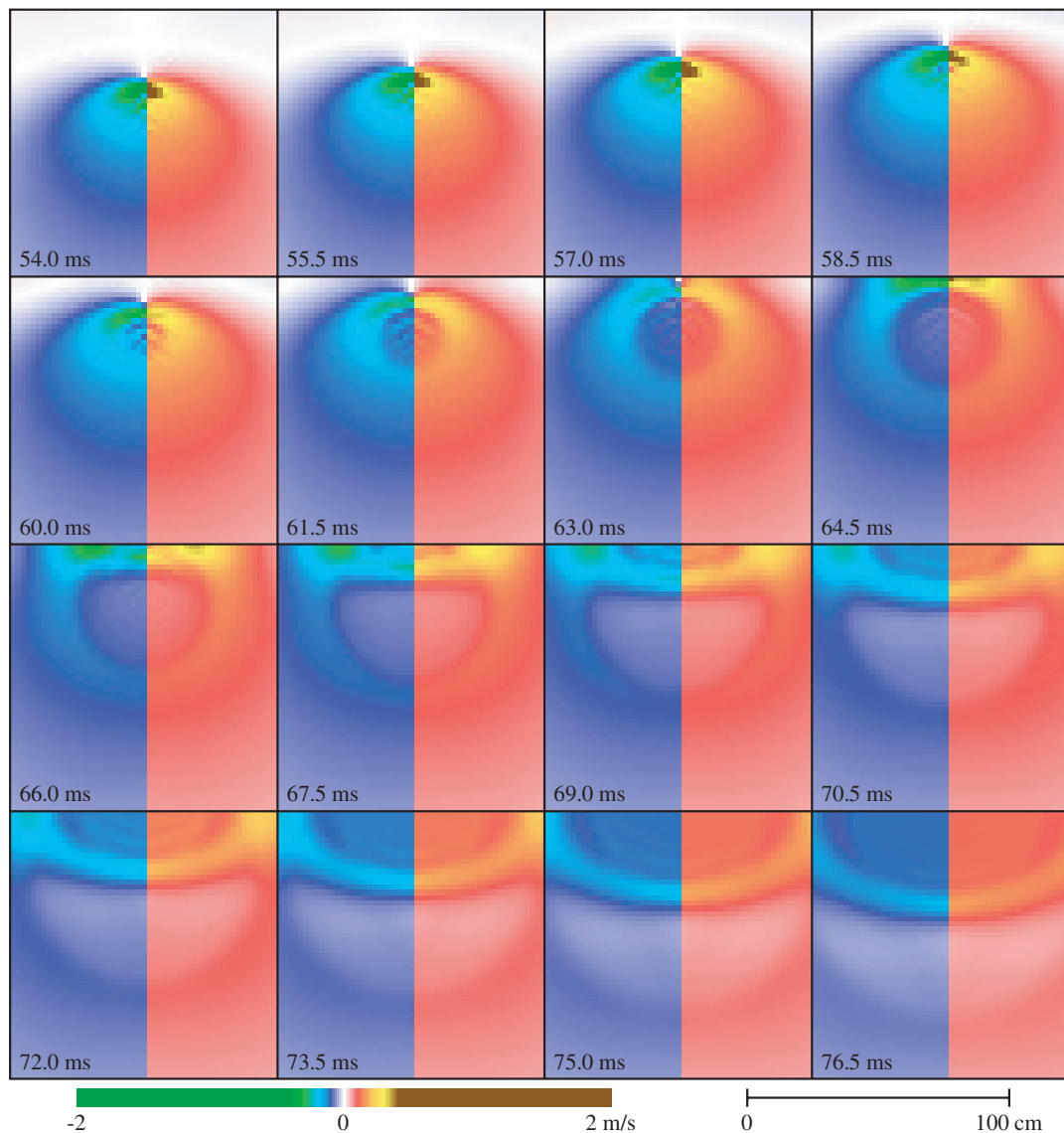


Figure 16. Cross-sectional snapshot images of along-strike particle velocity for the case with a 20-cm weak zone and modified μ_w value (0.4).

comparisons have provided support for the validity of this procedure.

A demonstration of numerical convergence, that is, achieving nearly identical numerical results using progressively finer gridding of the continuum and fault plane, might seem to be a more straightforward and flexible way of validating the numerical model. However, even given sufficient computing resources to refine the grid indefinitely, numerical convergence alone may not validate the accuracy of a discrete solution for nonlinear problems of this sort. A classic counterexample is the behavior of solutions to the upstream finite-difference approximation to the advective form of the generalized Burger's equation with discontinuous initial conditions (e.g., Durran, 1999, pp. 241–243). The numerical solution is stable and converges nicely as the spatial grid interval Δx is reduced, producing a shock front. Unfor-

tunately, relative to the known exact (weak) solution, the numerical solution still has a completely incorrect propagation velocity in the limit of arbitrarily small Δx . Thus, numerical convergence is a necessary, but by no means sufficient, condition for convergence to the continuum solution. The existence of such counterexamples underscores the unique role that scale-model experiments can play in demonstrating solution validity in the spontaneous rupture problem.

Conclusions

Numerical simulations of the scale-model earthquake experiments of Brune and Anooshehpour (1998) demonstrate the accuracy of a numerical solution method employed in previous studies of spontaneous rupture propagation (e.g.,

Day, 1982). The numerical simulations faithfully reproduce the shape and duration of the acceleration pulses recorded adjacent to the model fault surface, both with and without a weak strip along the top part of the fault plane. The comparison of the numerical solutions and experimental records validates the numerical method in a way that could have been achieved neither through comparisons with analytical solutions nor through numerical demonstrations of grid-interval invariance. The comparison with scale-model experimental data does not by itself demonstrate relevance of the numerical model to natural earthquakes but does provide a basis for validation of the numerical method that is in many respects superior to earthquake data. Among the advantages realized from the use of experimental data are optimal sensor locations, precise knowledge of bulk and surface properties of the medium, detailed knowledge of the initial state, and experimental repeatability.

The simulations also shed further light on the foam rubber experiments. The agreement of the numerical solutions with the experimental data supports an interpretation that the foam rubber events are predominantly frictional sliding events, with most, if not all, of the fault displacement occurring with the fault faces in frictional contact. The result is a cracklike mode of slip in the foam model of Brune and Anooshehpour (1998), rather than the pulselike behavior suggested by earlier experiments (Brune *et al.*, 1993). The apparently high rupture velocity in the weak zone is most likely an artifact of the slight sensor offset from the fault, with the actual rupture slowing upon encountering the weak zone. Finally, the numerical simulations predict that the weak zone diminishes surface accelerations and velocities (relative to a uniform fault model) out to a distance that scales with weak-zone depth, beyond which its effect is small. The weak zone may even enhance amplitudes slightly at intermediate distances.

Acknowledgments

We thank Rasool Anooshehpour and James Brune for providing experimental records from their foam rubber model and for many discussions of the experimental details that were essential to this study. We thank D. Joe Andrews and Raul Madariaga, whose reviews helped us improve the manuscript. This work was supported by the Los Alamos National Laboratory (U.S. DOE contract No. W-7405-ENG-36) and the Southern California Earthquake Center (SCEC). SCEC is funded by NSF Cooperative Agreement EAR-8920136 and USGS Cooperative Agreements 14-08-0001-A0899 and 1434-HQ-97AG01718. The SCEC Contribution Number for this article is 614.

References

- Andrews, D. J. (1976). Rupture propagation with finite stress in antiplane strain, *J. Geophys. Res.* **81**, 3575–3582.
- Andrews, D. J. (1999). Test of two methods for faulting in finite-difference calculations, *Bull. Seism. Soc. Am.* **89**, 931–937.
- Anooshehpour, A., and J. N. Brune (1994). Frictional heat generation and seismic radiation in a foam rubber model of earthquakes faulting, friction, and earthquake mechanics. I, *Pageoph* **142**, 735–747.
- Archuleta, R. J., and S. M. Day (1980). Dynamic rupture in a layered medium: the 1966 Parkfield earthquake, *Bull. Seism. Soc. Am.* **70**, 671–689.
- Broberg, K. B. (1999). *Cracks and Fracture*, Academic Press, San Diego.
- Brune, J. N., and A. Anooshehpour (1998). A physical model of the effect of a shallow weak layer on strong ground motion for strike-slip ruptures, *Bull. Seism. Soc. Am.* **88**, 1070–1078.
- Brune, J. N., S. Brown, and P. A. Johnson (1993). Rupture mechanism and interface separation in foam rubber models of earthquakes: a possible solution to the heat flow paradox and the paradox of large overthrusts, *Tectonophysics* **218**, 59–67.
- Brune, J. N., P. A. Johnson, and C. Slater (1990). Nucleation, predictability, and rupture mechanism in foam rubber models of earthquakes, *J. Himalayan Geol.* **1**, 155–166.
- Day, S. M. (1982). Three-dimensional simulation of spontaneous rupture: the effect of nonuniform prestress, *Bull. Seism. Soc. Am.* **72**, 1881–1902.
- Day, S. M., G. Yu, and D. J. Wald (1998). Dynamic stress changes during earthquake rupture, *Bull. Seism. Soc. Am.* **88**, 512–522.
- Dieterich, J. H. (1979). Modeling of rock friction. I. Experimental results and constitutive equations, *J. Geophys. Res.* **84**, 2161–2168.
- Dieterich, J. H. (1986). A model for the nucleation of earthquake slip, in *Earthquake Source Mechanics*, S. Das, J. Boatwright, and C. H. Scholz (Editors), American Geophysical Monograph 37, 37–47.
- Durrant, D. R. (1999). *Numerical Methods for Wave Equations in Geophysical Fluid Dynamics*, Springer-Verlag, New York.
- Freund, L. B. (1990). *Dynamic Fracture Mechanics*, Cambridge Univ. Press, Cambridge, U.K.
- Gerstenberger, M., S. Wiemer, and D. Giardini (2001). A systematic test of the hypothesis that the *b* value varies with depth in California, *Geophys. Res. Lett.* **28**, 57–60.
- Harris, R. A., and S. M. Day (1993). Dynamics of fault interaction: Parallel strike-slip faults, *J. Geophys. Res.* **98**, 4461–4472.
- Harris, R. A., and S. M. Day (1997). Effects of a low-velocity zone on a dynamic rupture, *Bull. Seism. Soc. Am.* **87**, 1267–1280.
- Harris, R. A., and S. M. Day (1999). Dynamic three-dimensional simulations of earthquakes on en echelon faults, *Geophys. Res. Lett.* **26**, 2089–2092.
- Harris, R. A., R. J. Archuleta, and S. M. Day (1991). Fault steps and the dynamic rupture process: 2-D numerical simulations of a spontaneously propagating shear fracture, *Geophys. Res. Lett.* **18**, 893–896.
- Harris, R. A., J. F. Dolan, R. Hartleb, and S. M. Day (2002). The 1999 Izmit, Turkey earthquake: a 3D dynamic stress transfer model of intra-earthquake triggering, *Bull. Seism. Soc. Am.* **92**, no. 1, 245–255.
- Ida, Y. (1972). Cohesive force across the tip of a longitudinal-shear crack and Griffith's specific surface energy, *J. Geophys. Res.* **77**, 3796–3805.
- Ide, S., and M. Takeo (1997). Determination of constitutive relations of fault slip based on seismic wave analysis, *J. Geophys. Res.* **102**, 27,379–27,391.
- Kilgore, B. D., M. L. Blanpied, and J. H. Dieterich (1993). Velocity dependent friction of granite over a wide range of conditions, *Geophys. Res. Lett.* **20**, 903–906.
- Madariaga, R., K. B. Olsen, and R. J. Archuleta (1998). Modeling dynamic rupture in a 3-D earthquake fault model, *Bull. Seism. Soc. Am.* **88**, 1182–1197.
- Magistrale, H., and S. M. Day (1999). Three-dimensional simulations of multisegment thrust fault rupture, *Geophys. Res. Lett.* **26**, 2093–2096.
- Marone, C. (1998). Laboratory-derived friction laws and their application to seismic faulting, *Ann. Rev. Earth Planet. Sci.* **26**, 643–696.
- Marone, C., and C. H. Scholz (1988). The depth of seismic faulting and the upper transition from stable to unstable slip regimes, *Geophys. Res. Lett.* **15**, 621–624.
- Miyatake, T. (1980). Numerical simulations of earthquake source process by a three-dimensional crack model. I. Rupture Process, *J. Phys. Earth* **28**, 565–598.

- Mori, J., and R. E. Abercrombie (1997). Depth dependence of earthquake frequency-magnitude distributions in California: implications for rupture initiation, *J. Geophys. Res.* **102**, 15,081–15,090.
- Oglesby, D. D., and S. M. Day (2003). Stochastic fault stress: implications for fault dynamics and ground motion, *Bull Seism. Soc. Am.* (in press).
- Okubo, P. G. (1989). Dynamic rupture modeling with laboratory-derived constitutive relations, *J. Geophys. Res.* **94**, 12,321–12,335.
- Olsen, K. B., R. Madariaga, and R. J. Archuleta (1997). Three-dimensional dynamic simulation of the 1992 Landers earthquakes, *Science* **278**, 834–838.
- Ruina, A. (1983). Slip instability and state variable friction laws, *J. Geophys. Res.* **88**, 10,359–10,370.
- Stevens, J. L., and S. M. Day (1985). The physical basis of m_b , M_s , and variable frequency magnitude methods for earthquake/explosion discrimination, *J. Geophys. Res.* **90**, 3009–3020.

Dept. of Geological Sciences
San Diego State University
San Diego, California 92182

Manuscript received 23 October 2001.